Supplementary Information (SI) for Nanoscale Horizons.
This journal is © The Royal Society of Chemistry 2025

Unveiling Giant Polarization Ratio of Chiral Photoluminescence in MoS_2 Nanorolligami Fabricated by Center-to-edge Rolling Mechanism

Rahul Kesarwani[1, 2], Miroslav Veverka[1], Martin Žáček[1], Vaibhav Varade[1], Ladislav Fekete[3], Martin Kalbac[2], and Jana Vejpravova[1]*

[1] Department of Condensed Matter Physics, Faculty of Mathematics and Physics, Charles University, Ke Karlovu 5, 121 16 Prague 2, Czech Republic

[2] Department of Low-Dimensional Systems, J. Heyrovsky Institute of Physical Chemistry, Dolejskova 3, 182 23 Prague 8, Czech Republic

[3] Department of Analysis of Functional Materials, Institute of Physics of the Czech Academic of Sciences, Na Slovance 2, 182 00 Prague 8, Czech Republic

*Email: jana.vejpravova@matfyz.cuni.cz

Keywords: Photoluminescence, Raman Spectroscopy, Light-matter Interaction, Circular Polarisation, Transition Metal Dichalcogenides, Nanorolligami, Optical Anisotropy

This file includes:

Movie- M1 to M3

Figures. – S1 to S14

Note- 1

Tables- S1 to S2

References

1. **Movie to show the rolling of monolayer (1-L) MoS_2.**

M1. This movie shows how the aged 1-L MoS_2 started rolling while reacting with the solution of water and ethanol in the ratio of 2:1. The whole movie has been captured using a charged-couple device (CCD) camera attached to an optical microscope (OM).

SI\aged MoS_2 sample.mp4

M2. This movie shows how the 24-hour styrene exposed 1-L MoS_2 started rolling while reacting with the same concentrate solution.

SI\24 hr exposed MoS_2 sample.mp4

M3. This movie shows how the fresh sample of 1-L MoS_2 started rolling while reacting with the same concentrate solution.

SI\Fresh MoS_2 sample.mp4

2. Optical images of styrene exposed and as-deposited MoS_2 samples.

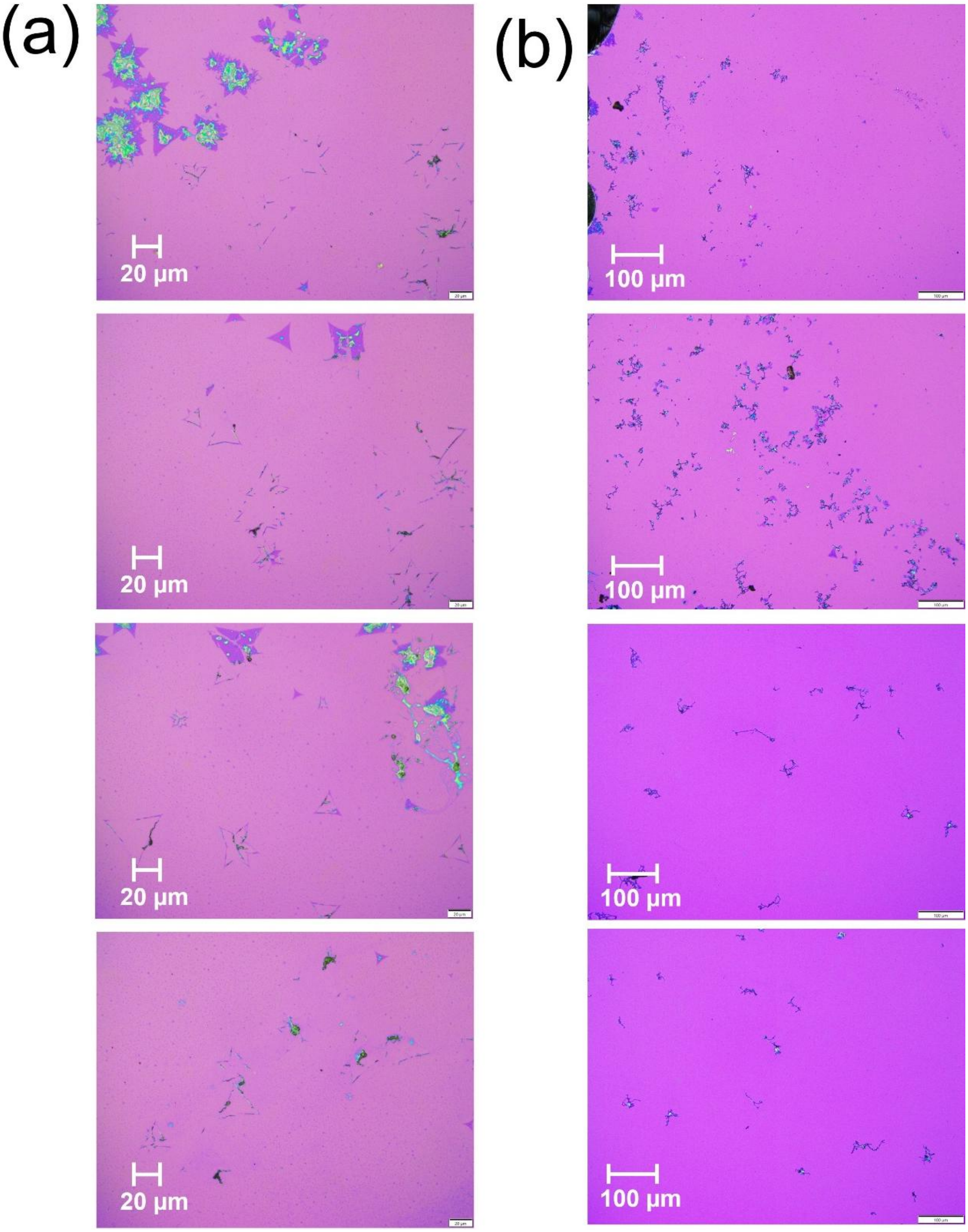

Figure S1: **Optical images of nanorollingami of MoS_2**. (a) styrene exposed and (b) as deposited. The images reveal that the styrene-exposed rolled MoS_2 exhibits a more organized and uniform rolling behaviour compared to the as-deposited rolled MoS_2.

3. Atomic force microscopic (AFM) of styrene exposed and as-deposited MoS_2 samples.

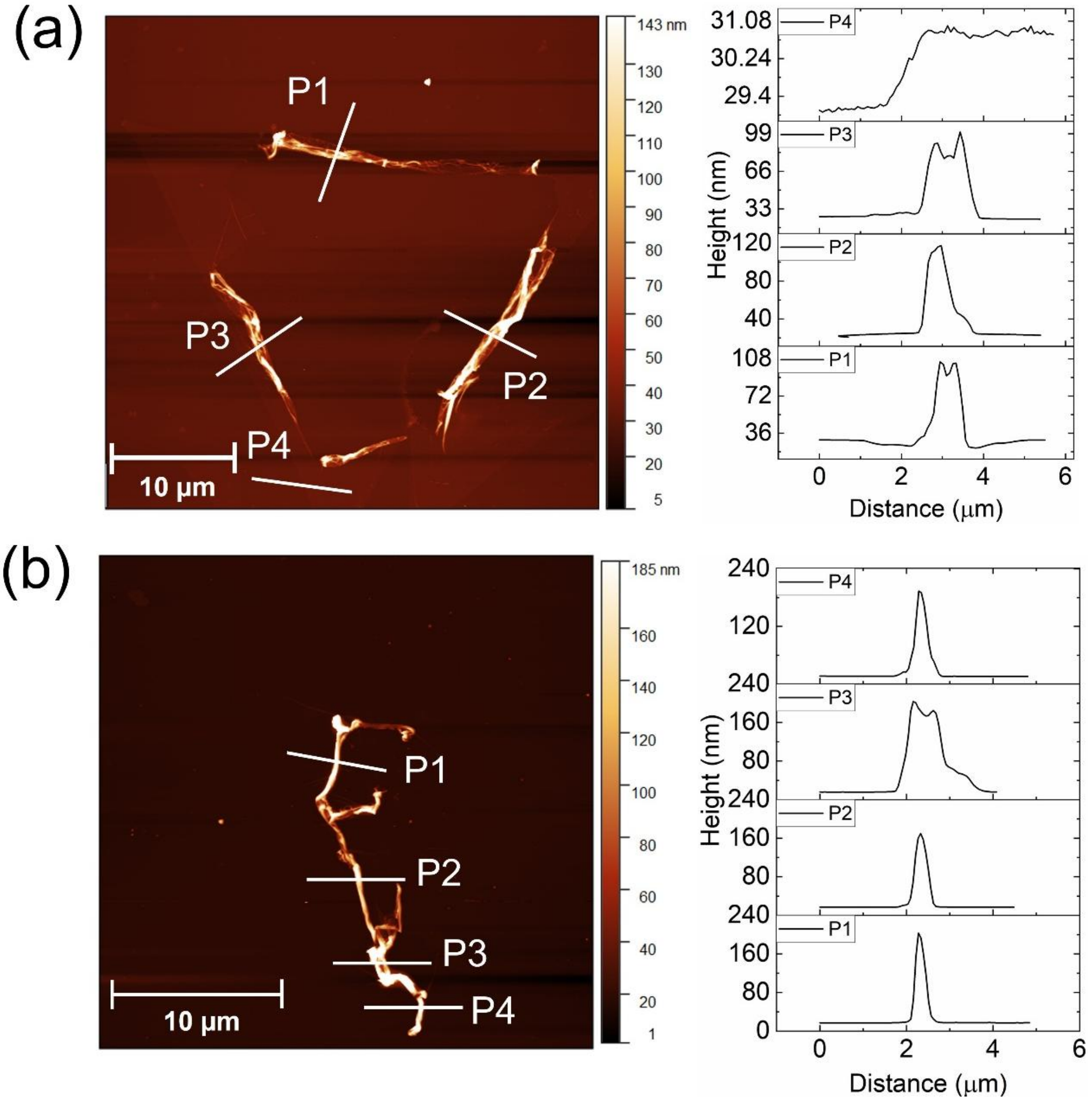

Figure S2: **AFM images of styrene exposed and as-deposited nanorollingami MoS_2.** (a) AFM image of styrene-exposed nano rolled MoS_2 with height profiles drawn at four different positions (P1 to P4). Positions P1 to P3 correspond to nanorolled regions, while P4 represents the flat (correspond to monolayer) MoS_2 in the same sample. (b) AFM image of as-deposited nanorolled MoS_2 with height profiles similarly drawn at four positions. Notably, for the styrene-exposed sample, interaction with a water+ethanol solution induces rolling behavior similar to aged samples, showing breaks from the center and rolling towards each corner, while maintaining intact monolayer regions. In contrast, the as-deposited sample exhibits higher surface roughness and random crumpling after solution interaction.

4. Optical AFM images along with height profile of aged MoS$_2$ sample.

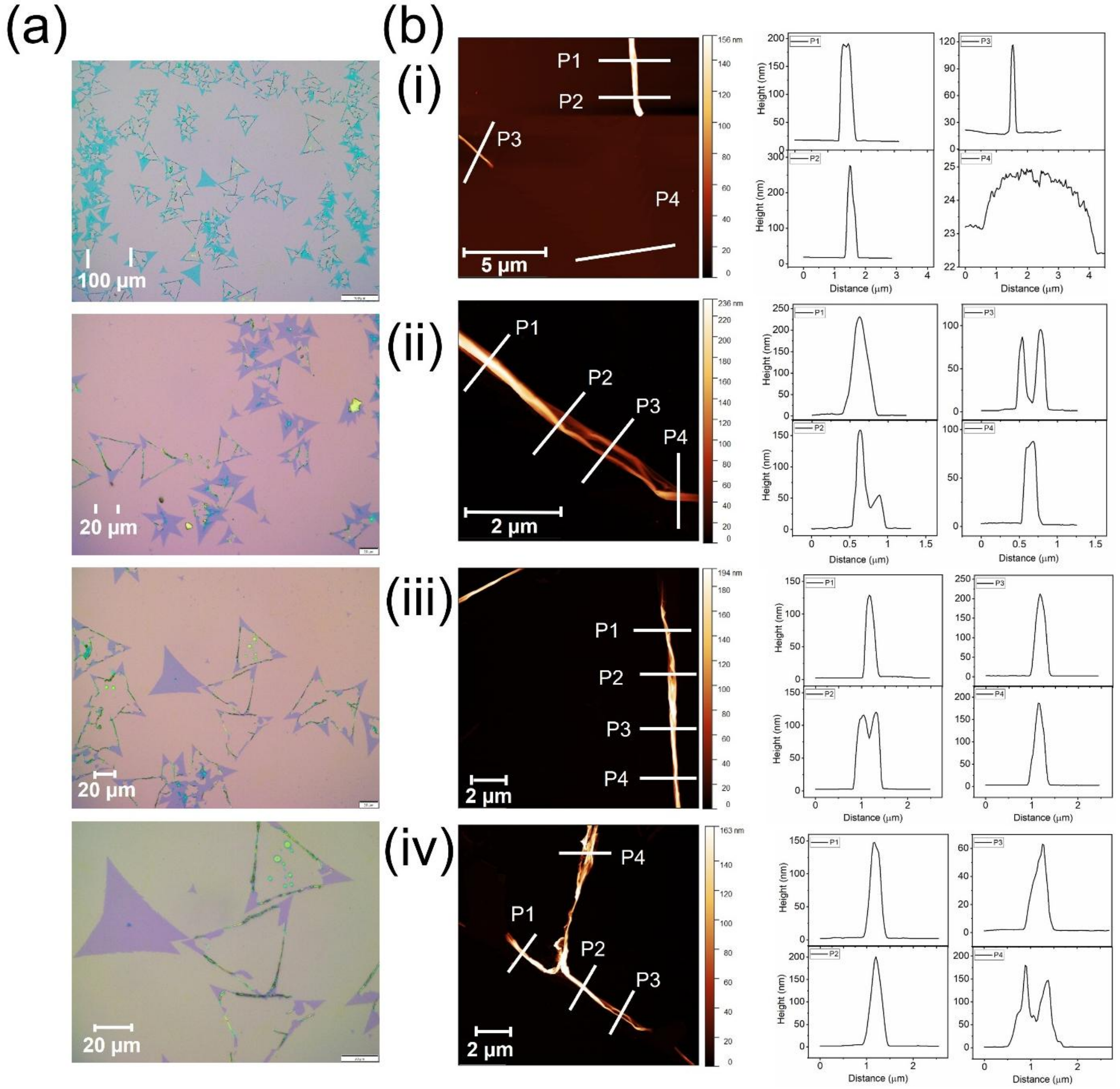

Figure S3: **Optical image and height profile of aged nanorollingami MoS$_2$**. (a) Optical images of different parts of the aged MoS$_2$ rolled sample demonstrate the uniformity of the rolling behavior throughout the sample. Upon interaction with the solution, the rolling begins with a break at the center and extends systematically toward the corners. This consistent rolling pattern across various regions validates the uniform effect of the solution-induced interaction on the aged MoS$_2$ sample. (b) Height profiles of the rolled MoS$_2$ sample are analyzed for different regions to understand the variations in thickness and crumpling: (i) A combined height profile of regions R1 to R3 is presented. Height variations are plotted at multiple positions, highlighting the morphological differences across the combined area. (ii) For region R2, height profiles drawn at various positions reveal significant variations, ranging from 110 nm to 220 nm. The lower part of this region shows noticeable random crumpling, which contributes to the observed height variation. (iii) Region R3 is analyzed at different positions, with thickness variations ranging from 100 nm to 200 nm. Increased crumpling is observed at the triangular corners of this region, which is consistent across all three corners, indicating localized mechanical stress during rolling. (iv) Height profiles of other regions are compiled to support the broader observation that crumpling intensifies near the corners of the rolled structure. This crumpling contributes to significant thickness variations in these corner regions, which is a recurring feature across the aged MoS_2 sample. These observations collectively confirm that the solution react induces a characteristic rolling pattern accompanied by crumpling, particularly concentrated at the corners, leading to distinct thickness variations.

5. Photoluminescence (PL) mapping of rolled MoS_2 sample under co-polarized light.

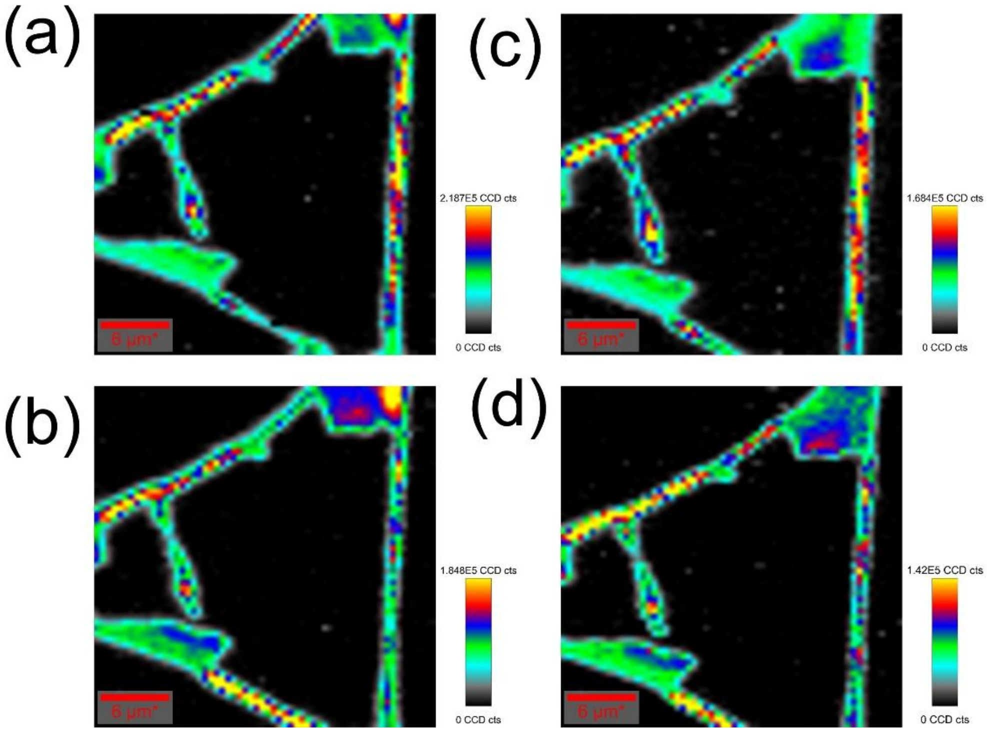

Figure S4: **PL mapping of a nanorollingami MoS_2 under different co-polarization states at room temperature (RT)**. (a) Horizontally polarized (HP) incident light with HP scattering (*XX* configuration). (b) Vertically polarized (VP) incident light with VP scattering (*YY* configuration). (c) Right circularly polarized (RCP) incident light with RCP scattering ($\sigma^+\sigma^+$ configuration). (d) Left circularly polarized (LCP) incident light with LCP scattering ($\sigma^-\sigma^-$ configuration). The PL mapping highlights distinct intensity variations across the monolayer and rolled regions. It is evident that the monolayer region exhibits lower PL intensity compared to the rolled regions, indicating changes in optical emission properties induced by the rolling process. Furthermore, the PL intensity is strongly dependent on the polarization state of the incident and scattered light. This dependence is visually apparent in the false color-coded PL maps, where each polarization state reveals a unique distribution of PL counts. The variations suggest that the polarization properties of the incident light significantly affect the optical response of the rolled MoS_2 regions, whereas their influence on the 1-L regions is minimal. These results underline the interplay between the structural modifications induced by rolling and the polarization-dependent optical properties of the material.

6. PL intensity ratio of co-polarized light at four different positions in the rolling sample and compared with 1-L MoS_2.

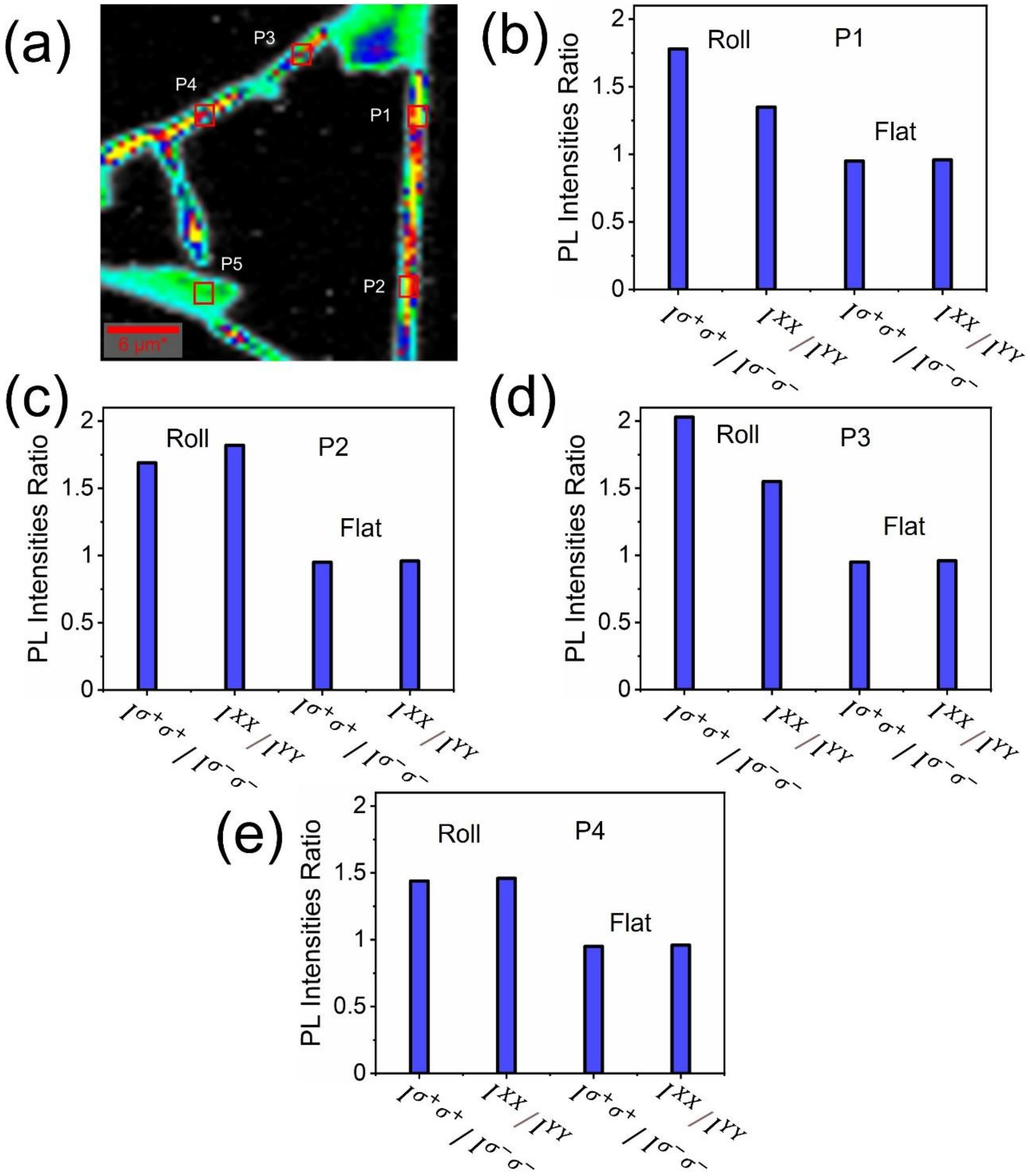

Figure S5: **PL Intensity ratio at different positions under co-polarized light**. (a) The PL mapping image shows the marked positions (P1 to P4 in the rolled regions and P5 in the flat region) where PL intensity ratios were estimated. For all rolled positions, the intensity ratios were compared to the flat region (P5). (b) to (e) present the calculated PL intensity ratios for circular and linear co-polarization, at positions P1 to P4, respectively. These ratios highlight the polarization-dependent differences in PL response between the rolled and flat regions. As shown, the PL intensity ratios for both circular and linear polarization are consistently higher in the rolled regions (P1 to P4) compared to the flat region (P5). This distinct difference indicates the formation of anisotropic optical behavior in the rolled regions, which contrasts with the isotropic nature of the flat (or 1-L). The higher intensity ratios in the rolled regions underscore the structural and optical modifications introduced during the rolling process, which leads to enhanced polarization sensitivity and anisotropy.

7. PL mapping of rolled MoS_2 sample under cross-polarized light.

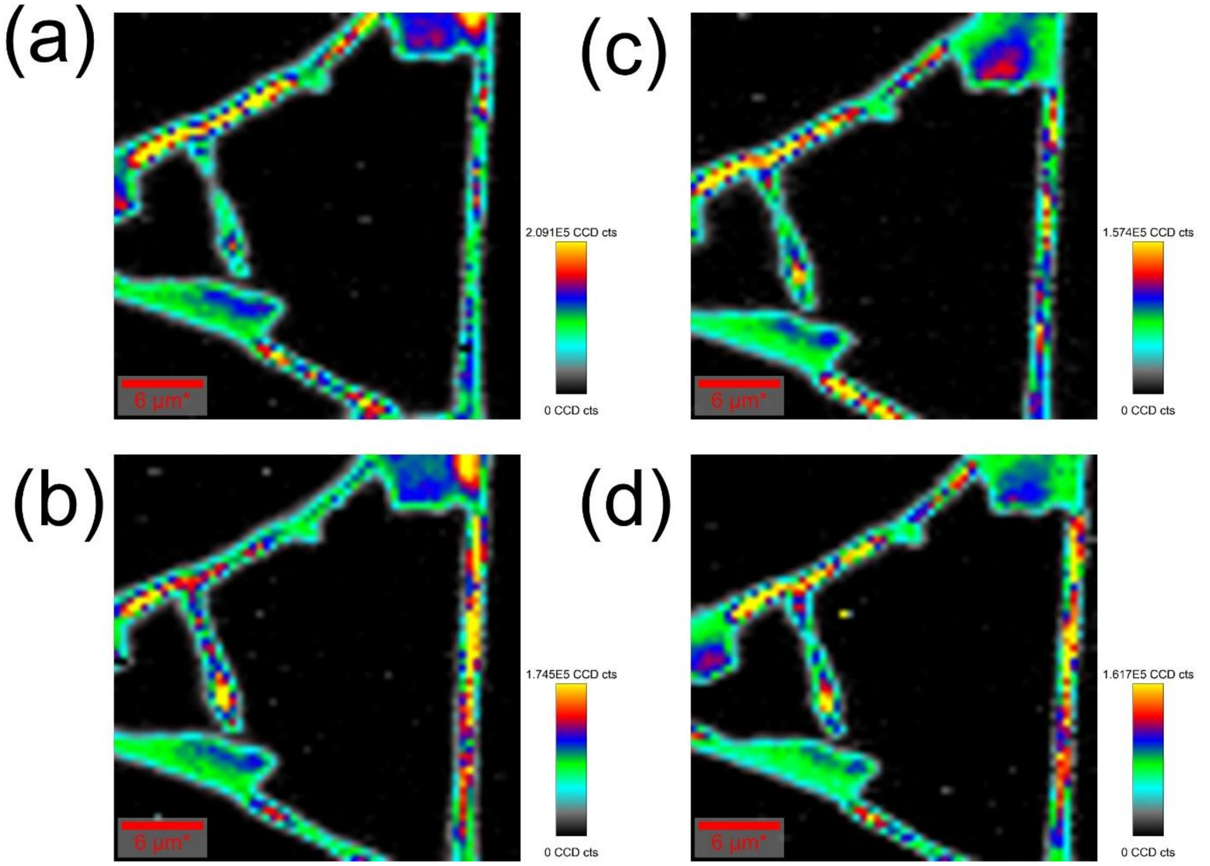

Figure S6: **PL mapping of a nanorollingami MoS_2 under different cross-polarization states at RT**. The polarization configurations are as follows: (a) Horizontally polarized (HP) incident light with vertically polarized (VP) scattered light (*XY* configuration). (b) VP incident light with HP scattered light (*YX* configuration). (c) Right circularly polarized (RCP) incident light with left circularly polarized (LCP) scattered light ($\sigma^{+}\sigma^{-}$ configuration). (d) LCP incident light with RCP scattered light ($\sigma^{-}\sigma^{+}$ configuration). Similar to the co-polarization results, the PL intensity is observed to be significantly higher in the rolled regions compared to the 1-L regions across all cross-polarization configurations. This consistent behavior across polarization states further highlights the distinct optical response of the rolled MoS_2 regions, potentially indicative of anisotropic properties introduced during the rolling process.

8. PL intensity ratio of cross-polarized light at four different positions in the rolling sample and compared with 1-L MoS$_2$.

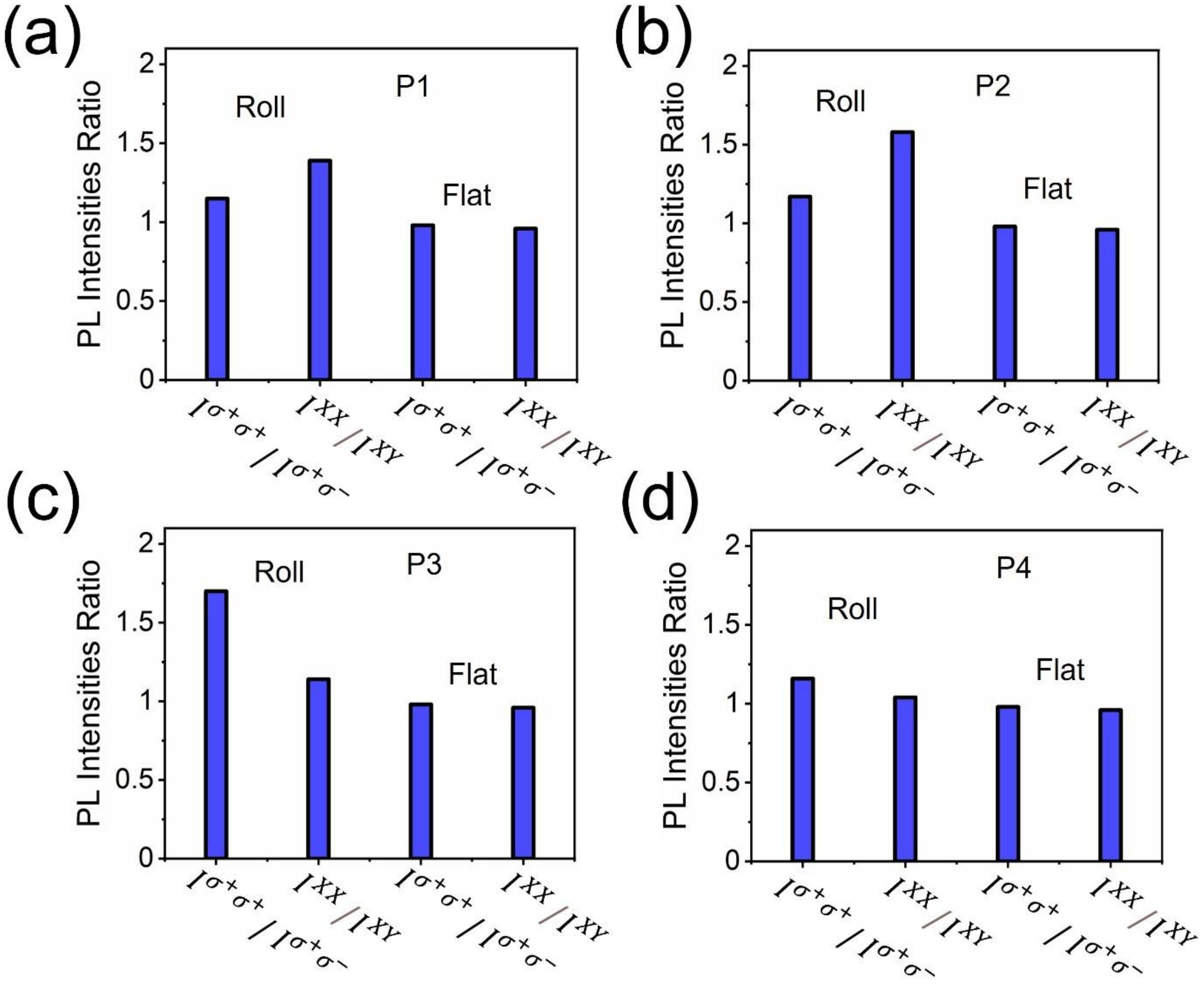

Figure S7: **PL intensity ratios at different positions under cross-polarized light**. (a) to (d) show the calculated PL intensity ratios for circular ($\sigma^+\sigma^-$ and $\sigma^-\sigma^+$) and linear (*XY* and *YX*) cross-polarization configurations at positions P1 to P4, respectively. The positions are marked in Fig. S6. Similar to the co-polarization case, the intensity ratios in the rolled regions (P1–P4) are consistently higher than in the flat reference region (P5). Although the differences in ratios between the rolled and flat regions are less pronounced under cross-polarization, the results still highlight the anisotropic optical response of the rolled regions induced by the rolling process.

9. Confirmation of no interlayer coupling through Raman and PL spectra.

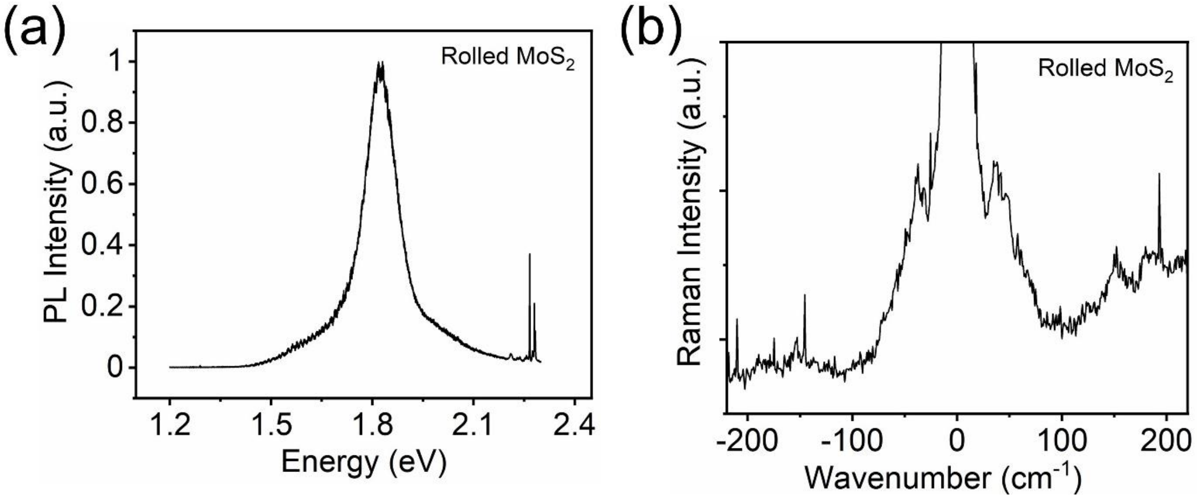

Figure S8: **Evidence of weak interlayer coupling in the nanorollingami MoS$_2$ at RT.** (a) The PL intensity of the rolled region is presented. If strong interlayer coupling were present, a broad peak around ~1.4 eV would be expected, as reported in previous literature[1]. However, this peak is not observed in the PL spectra of the rolled regions, indicating that the interlayer coupling effect is weak. This absence confirms that the layers in the rolled region do not exhibit significant coupling and likely behave as quasi-independent 1-Ls. (b) The Raman spectra of the rolled region are shown in the low-wavenumber range (< 100 cm^{-1}). Literature reports indicate that strong interlayer coupling results in multiple low-wavenumber peaks corresponding to shear and breathing modes[2]. In our observations, a faint and less intense peak near 35 cm^{-1} is detected only at very high power (> 500 µW), suggesting the presence of bulk-like MoS$_2$. However, at lower laser power (< 500 µW), no such peaks are observed. This behavior further supports the interpretation that the rolled layers exhibit weak interlayer coupling. The absence of significant low-wavenumber peaks under low power, which is characteristic of coupled multilayers, implies that each layer behaves independently, akin to 1-L MoS$_2$. This finding aligns with literature reports, where monolayers lack such low-wavenumber modes. These observations collectively confirm that the rolled regions maintain a weak interlayer coupling environment, preserving the quasi-monolayer nature of the structure. This has significant implications for the optical and vibrational properties of rolled MoS$_2$.

10. Verification of PL Intensity Independence from Valley Polarization.

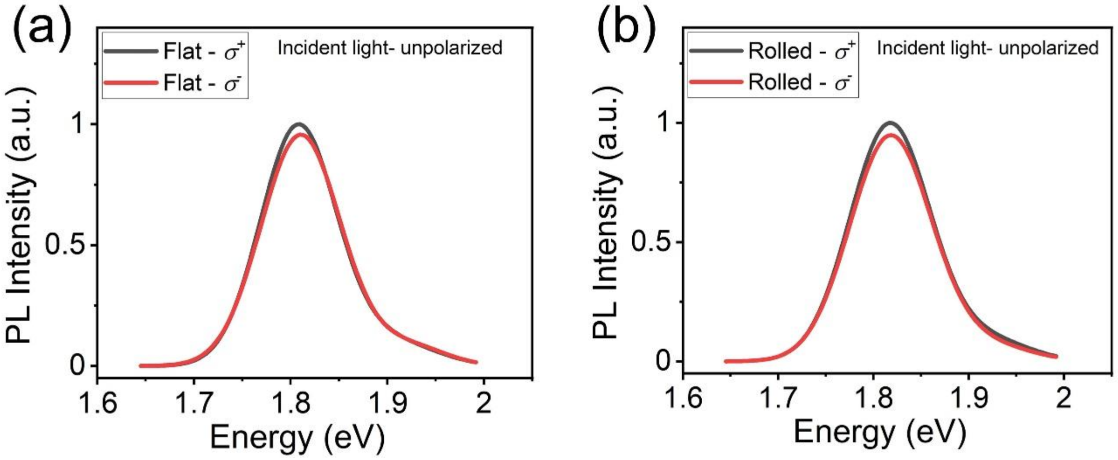

Figure S9: **Confirmation of No Valley Polarization Effect**. PL spectra of (a) flat and (b) rolled MoS_2 regions under unpolarized excitation, with detection in σ^+ and σ^- light. The identical PL intensity for both detection conditions in each region indicates that the PL intensity difference observed under $\sigma^+\sigma^+$ and $\sigma^-\sigma^-$ configurations (Fig. 3a and b) is not due to valley polarization. Instead, this result further supports the role of curvature-induced symmetry reduction and the varying orientation of individual layers in the rolled region, which influence the interaction with incident light properties.

11. Raman mapping of rolled MoS_2 sample under co-polarized light.

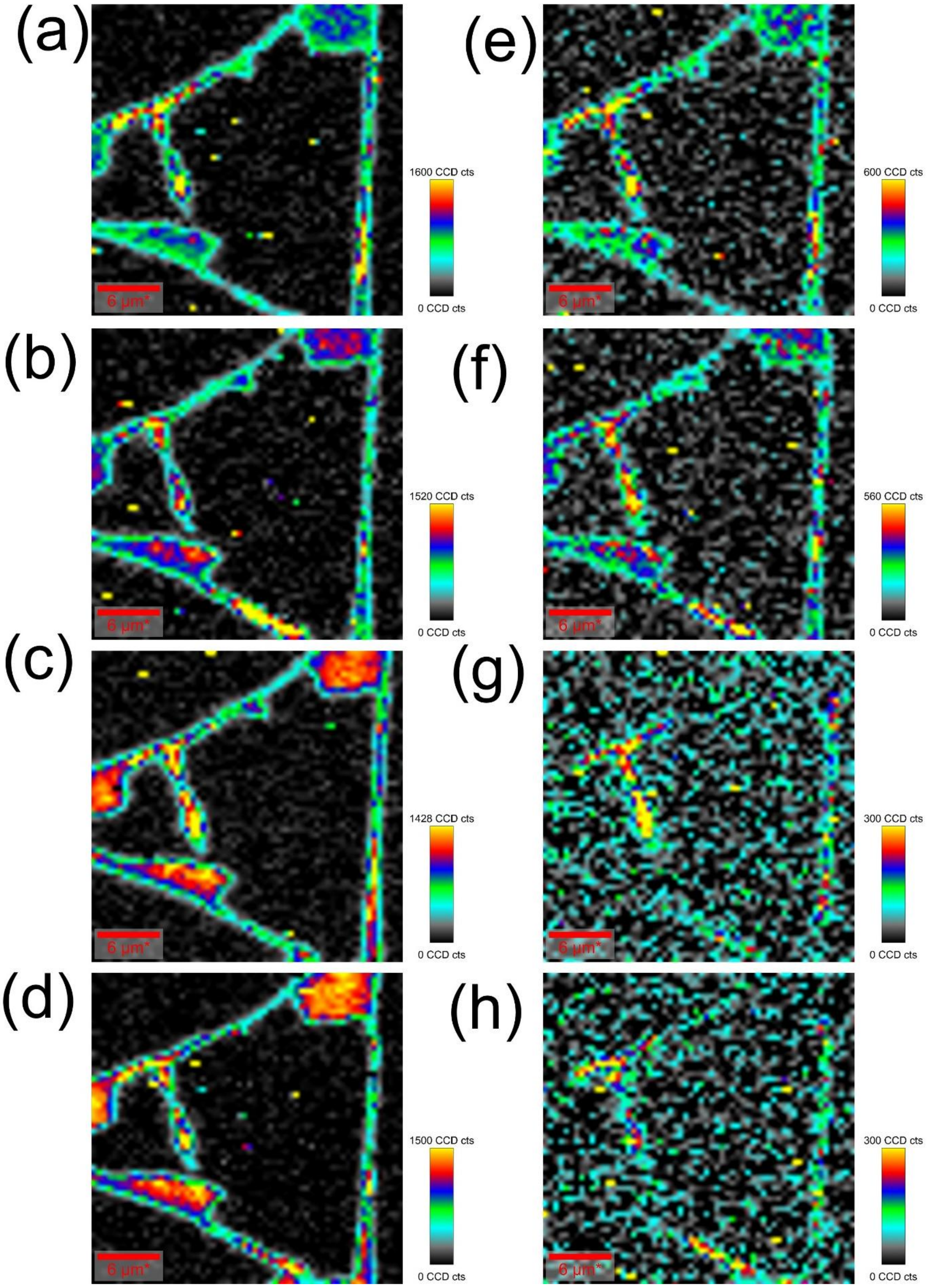

Figure S10: **Raman mapping of nanorollingami MoS_2 for A_{1g} and E_{2g} modes under different co-polarization states at RT.** (a) to (d) present the Raman mapping of the A_{1g} mode for co-polarized configurations of *XX*, *YY*, $\sigma^+\sigma^+$, and $\sigma^-\sigma^-$, respectively. Similarly, (e) to (h) present the Raman mapping of the E_{2g} mode for the same polarization states. From the Raman mapping, it is evident that under linear polarization conditions (*XX* and *YY*), both the A_{1g} and E_{2g} modes are activated in the rolled and flat regions, albeit with varying intensities. This indicates that linear polarization can effectively probe both in-plane and out-of-plane vibrational modes of the sample across different regions. In contrast, under circular polarization conditions ($\sigma^+\sigma^+$ and $\sigma^-\sigma^-$), a distinct behavior is observed. The A_{1g} mode is activated in both the rolled and 1-L regions, demonstrating sensitivity to circularly polarized light. However, the E_{2g} mode is only activated in the rolled regions and remains inactive in the flat regions under circular polarization. This stark difference between the activation of Raman modes in the rolled and flat regions highlights the influence of structural modifications induced by rolling on the polarization-dependent Raman response. The reasons behind these observations are discussed in detail in the manuscript, where the role of symmetry breaking and its impact on Raman mode activation in rolled and flat regions is thoroughly analyzed. These results emphasize the anisotropic optical behavior of the rolled regions compared to the isotropic response of the monolayer or flat regions under varying polarization states.

12. Raman mapping of rolled MoS_2 sample under cross-polarized light.

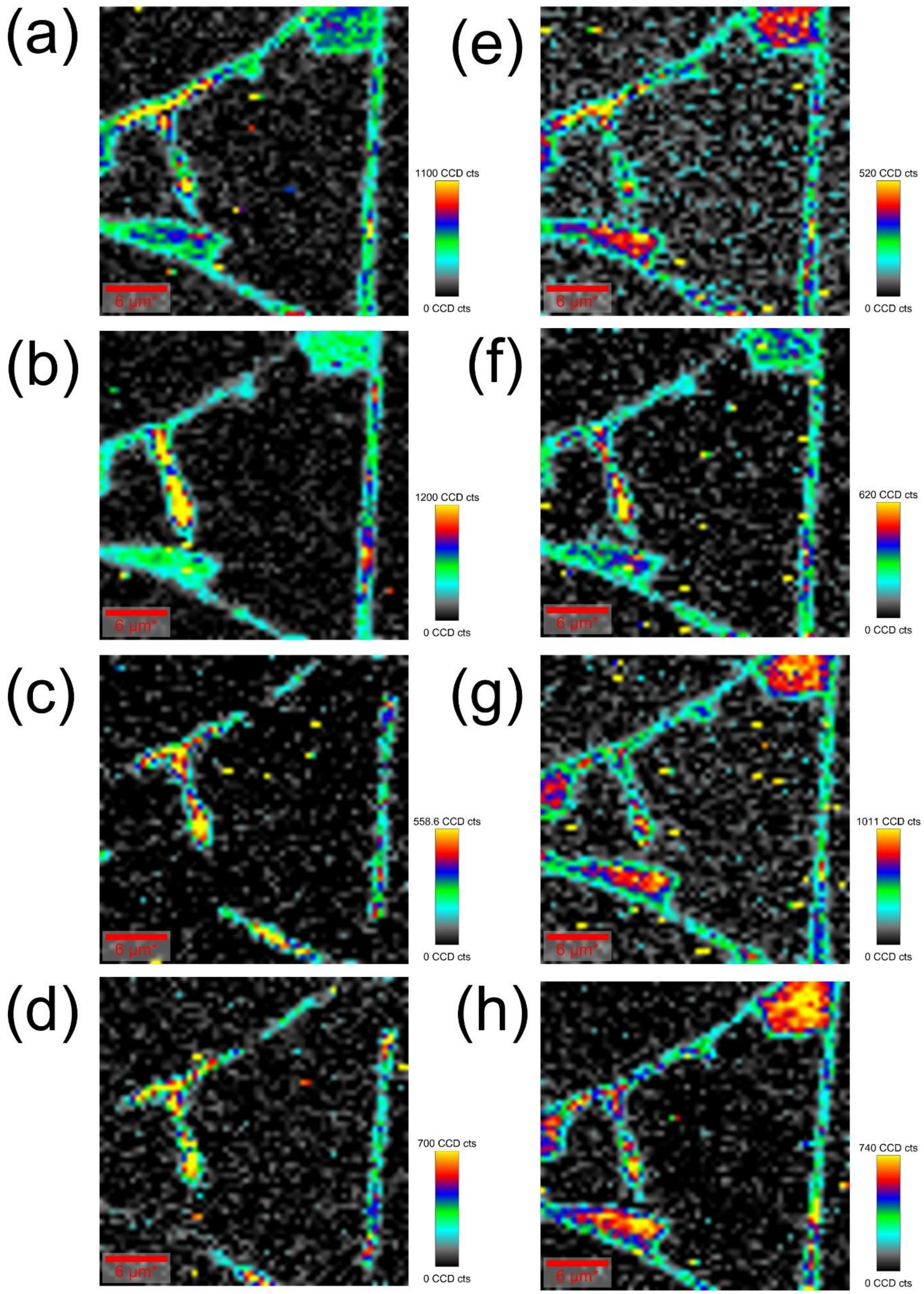

Figure S11: **Raman mapping of rolled $\mathbf{MoS_2}$ sample for $\mathbf{A_{1g}}$ and $\mathbf{E_{2g}}$ modes under different cross-polarization states at RT**. (a) to (d) present the Raman mapping of the A_{1g} mode for co-polarized configurations of XX, YY, $\sigma^+\sigma^-$, and $\sigma^-\sigma^+$, respectively. Similarly, (e) to (h) present the Raman mapping of the E_{2g} mode for the same cross-polarization states. Like the co-polarization case, the cross-polarization Raman mapping is evident that under linear cross-polarization conditions (XY and YX), both the A_{1g} and E_{2g} modes are activated in the rolled and 1-L regions, albeit with varying intensities. This indicates that linear polarization can effectively probe both in-plane and out-of-plane vibrational modes of the sample across different regions. The behavior is markedly different under circular cross-polarization ($\sigma^+\sigma^-$ and $\sigma^-\sigma^+$). The E_{2g} mode is activated in both the rolled and 1-L regions, indicating that it is sensitive to circularly polarized light in both areas. Conversely, the A_{1g} mode shows selective activation, being observed only in the rolled regions, while remaining inactive in the 1-L regions under these configurations. This selective behavior under circular cross-polarization further supports the hypothesis of structural and optical anisotropies induced by the rolling process, which influence the Raman response of the sample. The detailed reasons for the selective activation of phonon modes in the rolled regions, as observed in the cross-polarized case is the same as the co-polarization state, are thoroughly discussed in the manuscript and summarized in Figure S10.

13. PL Polar plots for two more distinct positions of linear and circular polarized light.

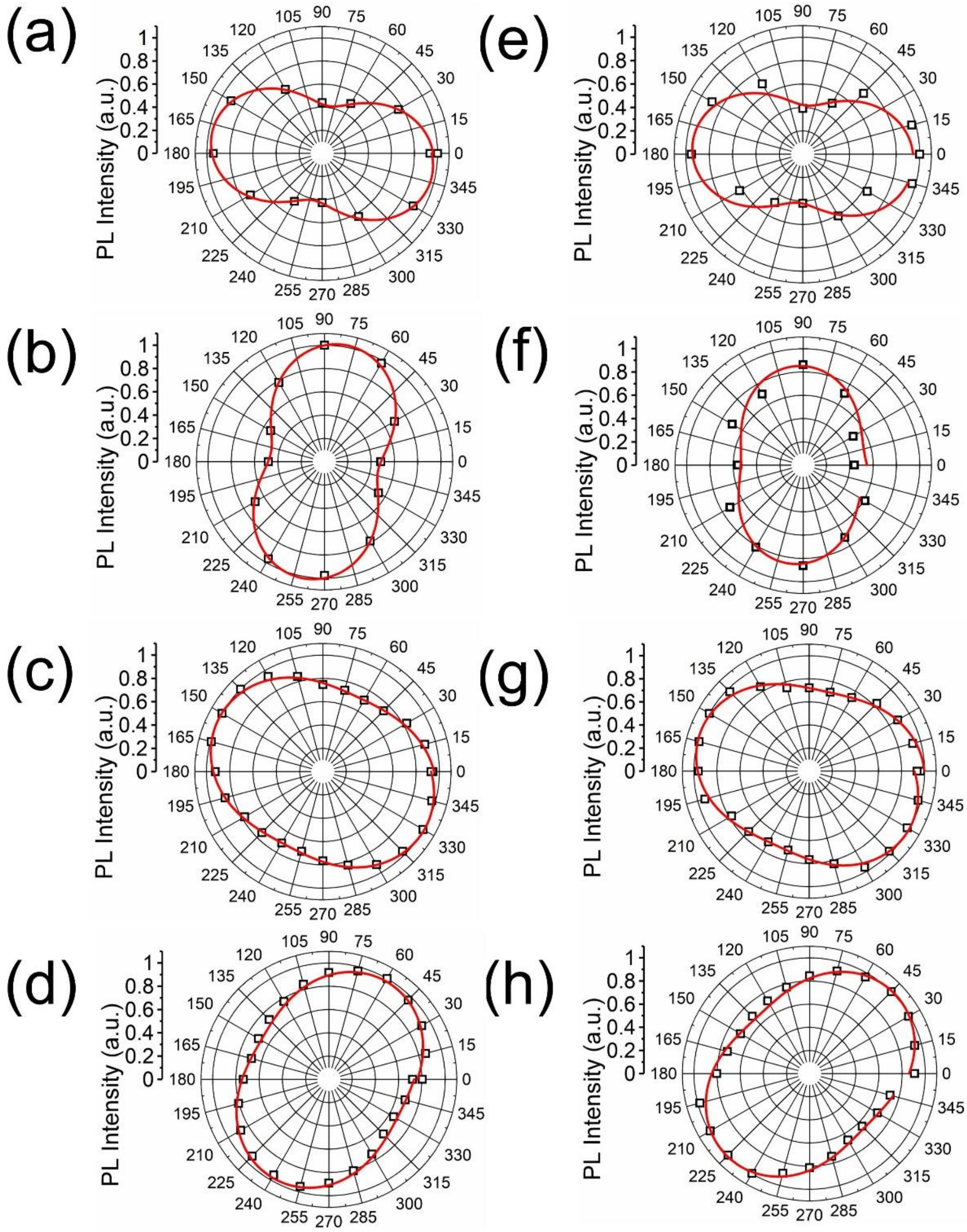

Figure S12: **PL angular characterization of nanorollingami.** Angular characterization is performed by varying the analyzer angles from 0º to 360º at 15º intervals to fix the plane of incident polarized light at RT. (a) to (d) and (e) to (h), show the angular PL intensity for the two distinct rolling regions, each excited by horizontal (*X*), vertical (*Y*), right circular (σ^{+}), and left circular (σ^{-}) polarized light, respectively.

14. Raman Polar plots for two more distinct positions of linear and circular polarized light.

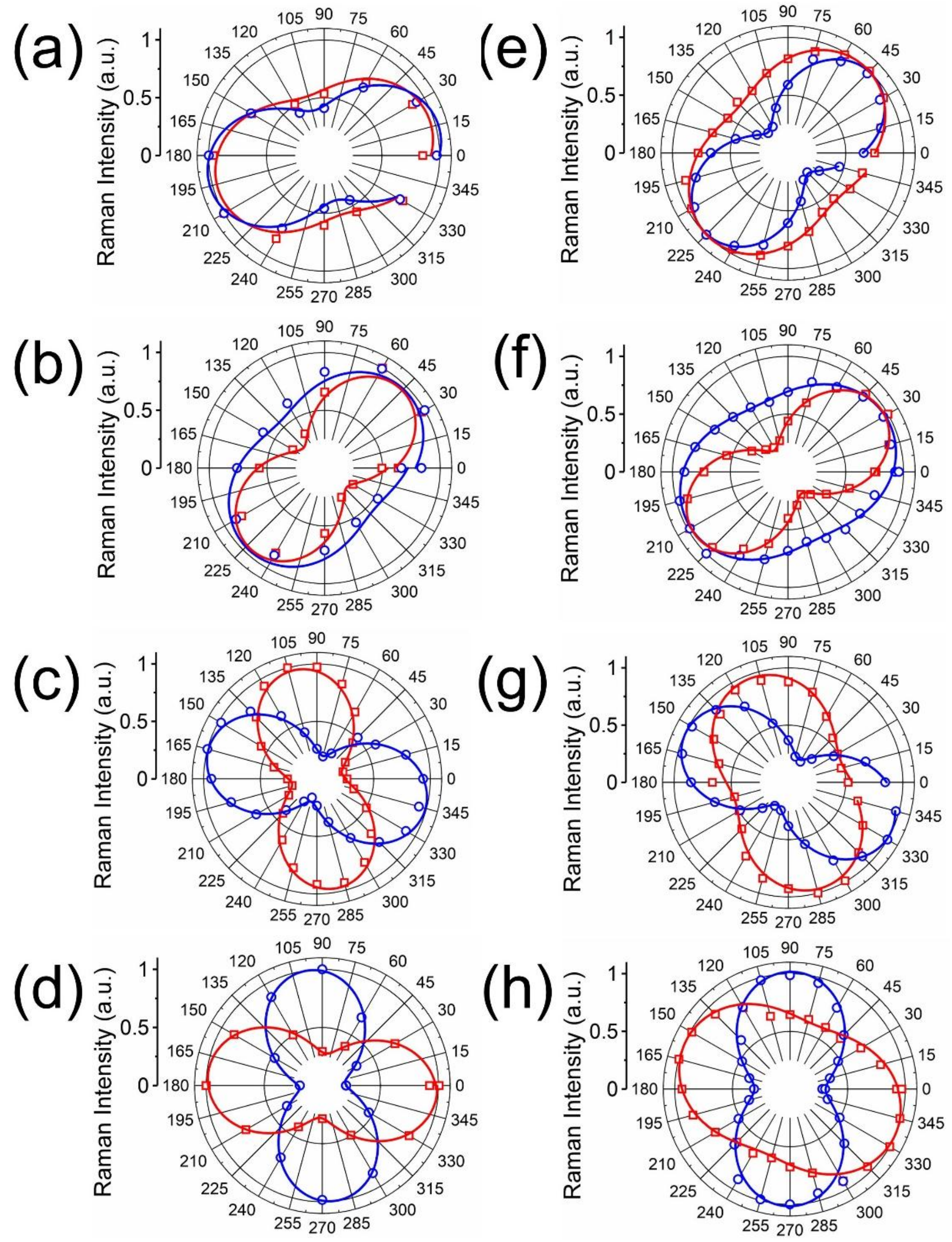

Figure S13: **Raman angular characterization of nanorollingami.** Angular measurements are performed similarly to the PL characterization. Square and circles correspond to the measured data of A_{1g} and E_{2g} modes, respectively. (a) to (d) and (e) to (h) show the angular Raman intensity for the two distinct rolling regions, each excited by horizontal (X), vertical (Y), right circular (σ^{+}), and left circular (σ^{-}) polarized light, respectively.

15. In-house experimental setup for Raman and PL measurements.

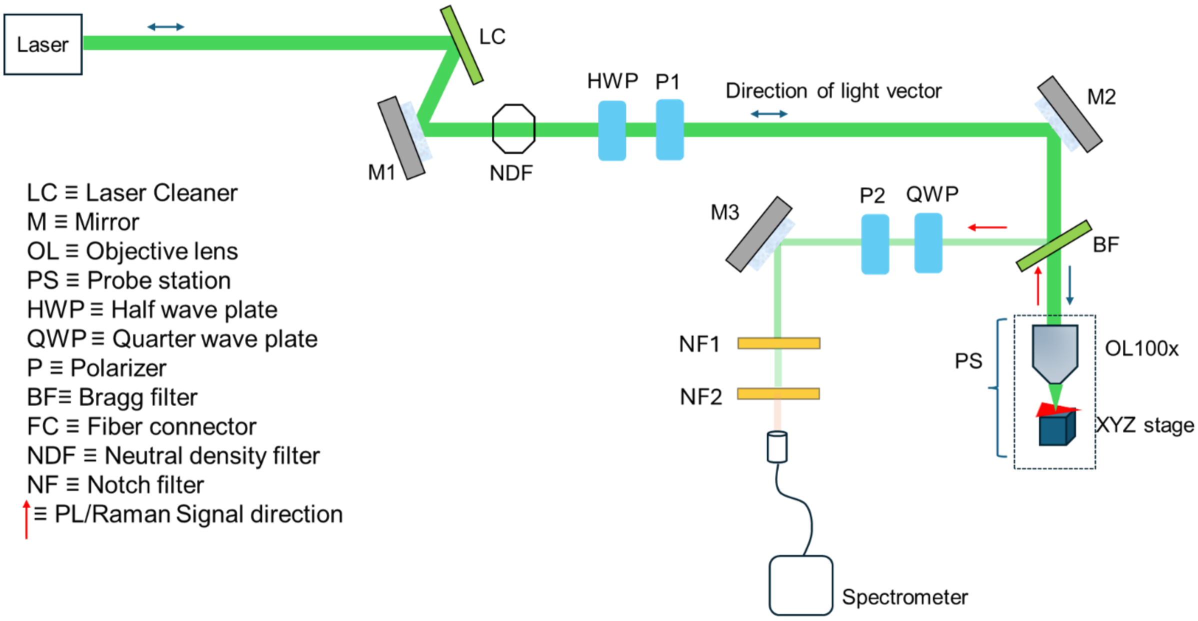

Figure S14: **Schematic diagram of in-house Raman and PL measurements**. A 100× objective lens (numerical aperture 0.82, lateral resolution of 500 nm) was used to focus the 532 nm (2.33 eV) laser excitation of linearly and circularly polarised light at 300 μW power. The outgoing signal was captured by the WITec alpha300R spectrometer, connected to the optical setup. The spectral resolution of the spectrometer under the measurement conditions using 600/1800 lines/cm grating, was 0.5 cm^{-1}.

16. **Note 1: Calculate the Raman tensors at different Euler's angles**.

When a 1-L MoS_2 sheet undergoes rolling, symmetry breaking occurs, leading to changes in the Raman tensors. As a result, phonon modes that are typically forbidden under circular polarization states become activated. The rolling process introduces a curved surface, where laser light interacts with different angles relative to the curved plane. This interaction can be interpreted using Euler's angle rotations, providing a framework for understanding the anisotropic behavior induced by rolling. Given that rolled MoS_2 behaves as a bulk material, we calculated the Raman tensors for different Euler angle orientations to simulate bulk 2H-MoS_2 (D_{6h} point group) and bulk 3R-MoS_2 (C_{3v} point group). The tensor values were derived from the Bilbao Crystallography Server (open access) [3-5]. Raman intensity calculations were performed for various incident light polarizations, including σ^+, σ^-, X, and Y polarizations, with the results summarized in Tables S1 and S2. The findings reveal that at $\psi' = 0$, corresponding to the flat region of the rolled MoS_2 (analogous to 1-L), the E_{2g} Raman mode is inactive under co-circular polarization states ($\sigma^+\sigma^+$ and $\sigma^-\sigma^-$). However, for co-linear polarization states (XX and YY), the E_{2g} mode exhibits a non-zero intensity. Interestingly, as the light interacts with the curved rolling surface (non-zero ψ' and φ' angles), the E_{2g} mode becomes activated for both circular and linear polarization states. This behavior is detailed in Tables S1 and S2, where calculations are presented for ψ', φ' and θ' angles of 0°, 15°, 30°, 45°, 60°, 75°, and 90° for both the 2H and 3R phases of bulk MoS_2. These results emphasize the impact of surface curvature and symmetry breaking on the activation of Raman modes in rolled MoS_2.

Raman tensor defined as-

$$R_n = \begin{pmatrix} a & b & c \\ d & e & f \\ ii & jj & k \end{pmatrix} \text{ or } R_n = \{\{a\, b\, c\}, \{d\, e\, f\}, \{ii\, jj\, k\}\}$$

Circular Polarization vectors:

For Right circular polarization, rcp ($\boldsymbol{e}_{\sigma^+}$):

$$\boldsymbol{e}_{\sigma^+} = \frac{1}{\sqrt{2}}\begin{pmatrix} 1 \\ i \\ 0 \end{pmatrix}$$

For Left circular polarization, lcp ($\boldsymbol{e}_{\sigma^-}$):

$$\boldsymbol{e}_{\sigma^-} = \frac{1}{\sqrt{2}}\begin{pmatrix} 1 \\ -i \\ 0 \end{pmatrix}$$

Linear Polarization vectors:

For Horizontal polarization, HP ($\boldsymbol{e}_X$):

$$\boldsymbol{e}_X = \begin{pmatrix} 1 \\ 0 \\ 0 \end{pmatrix}$$

For Vertical polarization, VP ($\boldsymbol{e}_Y$):

$$\boldsymbol{e}_X = \begin{pmatrix} 0 \\ 1 \\ 0 \end{pmatrix}$$

Intensity Calculation

The Raman intensity ***I*** is given by:

$$I(\theta) \propto |\boldsymbol{e}_S^{+}.\boldsymbol{R}_n.\boldsymbol{e}_i|^2 \ldots\ldots.\ (1)$$

Scattering rcp light:

$$\boldsymbol{e}_{S,\ \sigma^+}(\theta) = cos\theta.\boldsymbol{e}_{\sigma^+} + sin\theta.\boldsymbol{e}_{\sigma^-} = \frac{1}{\sqrt{2}}\begin{pmatrix} (cos\theta + sin\theta) \\ i(cos\theta - sin\theta) \\ 0 \end{pmatrix}$$

Scattering lcp light:

$$\boldsymbol{e}_{S,\ \sigma^-}(\theta) = cos\theta.\boldsymbol{e}_{\sigma^-} + sin\theta.\boldsymbol{e}_{\sigma^+} = \frac{1}{\sqrt{2}}\begin{pmatrix} (cos\theta + sin\theta) \\ i(sin\theta - cos\theta) \\ 0 \end{pmatrix}$$

Scattering HP light:

$$\boldsymbol{e}_{S,\ X}(\theta) = cos\theta.\boldsymbol{e}_X + sin\theta.\boldsymbol{e}_Y = \begin{pmatrix} cos\theta \\ sin\theta \\ 0 \end{pmatrix}$$

Scattering VP light:

$$\boldsymbol{e}_{S,\ Y}(\theta) = cos\theta.\boldsymbol{e}_Y + sin\theta.\boldsymbol{e}_X = \begin{pmatrix} sin\theta \\ cos\theta \\ 0 \end{pmatrix}$$

From equation (1)

1. **Raman intensity for rcp incident and angular scattering**:

$$I_{\sigma^+-\theta} \propto \frac{1}{4}\Big[\big((cos\theta + sin\theta)a + (cos\theta - sin\theta)e\big)^2 + \big((cos\theta + sin\theta)b + (sin\theta - cos\theta)d\big)^2\Big]$$

Case I: $\theta = 0$, *rcp* – incident and *rcp*- scattering: $I_{rcp-\theta} = I_{rcp-rcp\,\equiv\,\sigma^+\sigma^+}$

$$I_{\sigma^+\sigma^+} \propto \frac{1}{4}[(a+e)^2 + (b-d)^2] \ldots\ldots.\ (2)$$

Case II: $\theta = 90$, *rcp* – incident and *lcp*- scattering: $I_{rcp-\theta} = I_{rcp-lcp\,\equiv\,\sigma^+\sigma^-}$

$$I_{\sigma^+\sigma^-} \propto \frac{1}{4}[(a-e)^2 + (b+d)^2] \ldots\ldots (3)$$

2. **Raman intensity for lcp incident and angular scattering**:

$$I_{lcp-\theta} \propto \frac{1}{4}\left[\left((cos\theta + sin\theta)a + (cos\theta - sin\theta)e\right)^2 + \left((sin\theta - cos\theta)d + (cos\theta + sin\theta)b\right)^2\right]$$

Case I: $\theta = 0$, *lcp* – incident and *lcp*- scattering: $I_{lcp-\theta} = I_{lcp-lcp\,\equiv\,\sigma^-\sigma^-}$

$$I_{\sigma^-\sigma^-} \propto \frac{1}{4}[(a+e)^2 + (d-b)^2] \ldots\ldots (4)$$

Case II: $\theta = 90$, *lcp* – incident and *rcp*- scattering: $I_{lcp-\theta} = I_{lcp-rcp\,\equiv\,\sigma^-\sigma^+}$

$$I_{\sigma^-\sigma^+} \propto \frac{1}{4}[(a-e)^2 + (d+b)^2] \ldots\ldots (5)$$

3. **Raman intensity for HP incident and angular scattering**:

$$I_{HP-\theta} \propto [a^2cos^2\theta + d^2sin^2\theta]$$

Case I: $\theta = 0$, *HP* – incident and *HP*- scattering: $I_{HP-\theta} = I_{HP-VP\,\equiv\,XX}$

$$I_{XX} \propto a^2 \ldots\ldots\ldots\ldots\ldots\ldots (6)$$

Case II: $\theta = 90$, *HP* – incident and *VP*- scattering: $I_{HP-\theta} = I_{HP-VP\,\equiv\,XY}$

$$I_{XY} \propto d^2 \ldots\ldots\ldots\ldots\ldots\ldots (7)$$

4. **Raman intensity for VP incident and angular scattering**:

$$I_{VP-\theta} \propto [e^2cos^2\theta + b^2sin^2\theta]$$

Case I: $\theta = 0$, *VP* – incident and *VP*- scattering: $I_{VP-\theta} = I_{VP-VP\,\equiv YY}$

$$I_{YY} \propto e^2 \ldots\ldots\ldots\ldots\ldots\ldots (8)$$

Case II: $\theta = 90$, *VP* – incident and *HP*- scattering: $I_{VP-\theta} = I_{VP-HP\,\equiv YX}$

$$I_{YX} \propto b^2 \ldots\ldots\ldots\ldots\ldots\ldots (9)$$

Euler rotation for estimating the Raman tensor in a different orientation

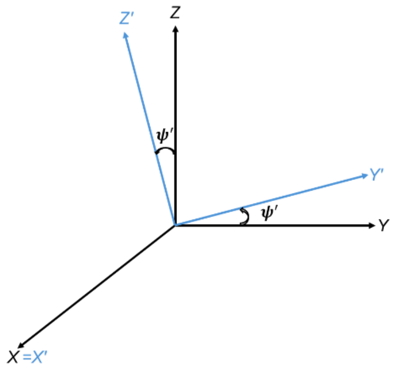

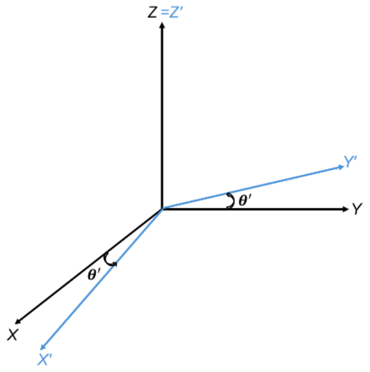

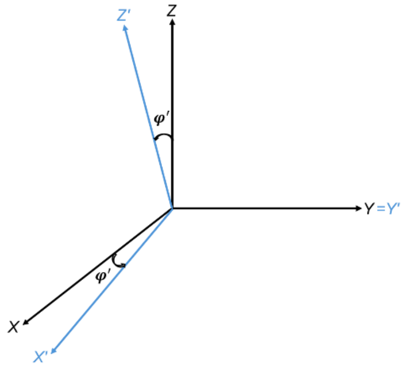

Table S1: $\boldsymbol{D}_{6h}$ (6/*mmm*) for bulk 2H-MoS$_2$

ψ'	$\mathbf{R}_n\ (A_{1g})$	$\sigma^+\sigma^+$	$\sigma^-\sigma^-$	XX	YY
0	$\{\{a',0,0\},\{0,a',0\},\{0,0,b'\}\}$	a'^2	a'^2	a'^2	a'^2
15	$\{\{a',0,0\},\{0,b',c'\},\{0,c',d'\}\}$	$(a'+b')^2$	$(a'+b')^2$	a'^2	b'^2
30	$\{\{a',0,0\},\{0,b',c'\},\{0,c',d'\}\}$	$(a'+b')^2$	$(a'+b')^2$	a'^2	b'^2
45	$\{\{a',0,0\},\{0,c',b'\},\{0,b',c'\}\}$	$(a'+c')^2$	$(a'+c')^2$	a'^2	c'^2
60	$\{\{a',0,0\},\{0,b',c'\},\{0,c',d'\}\}$	$(a'+b')^2$	$(a'+b')^2$	a'^2	b'^2
75	$\{\{a',0,0\},\{0,b',c'\},\{0,c',d'\}\}$	$(a'+b')^2$	$(a'+b')^2$	a'^2	b'^2
90	$\{\{b',0,0\},\{0,a',0\},\{0,0,b'\}\}$	$(a'+b')^2$	$(a'+b')^2$	b'^2	a'^2

ψ'	$\mathbf{R}_n\ (E_{2g})$	$\sigma^+\sigma^+$	$\sigma^-\sigma^-$	XX	YY
0	$\{\{d',0,0\},\{0,-d',0\},\{0,0,0\}\}$	0	0	d'^2	d'^2
15	$\{\{s',0,0\},\{0,k',l'\},\{0,l',m'\}\}$	$(s'+k')^2$	$(s'+k')^2$	s'^2	k'^2
30	$\{\{r',0,0\},\{0,s',k'\},\{0,k',l'\}\}$	$(s'+k')^2$	$(s'+k')^2$	r'^2	s'^2
45	$\{\{g',0,0\},\{0,r',h'\},\{0,h',r'\}\}$	$(g'+r')^2$	$(g'+r')^2$	g'^2	r'^2
60	$\{\{h',0,0\},\{0,r',s'\},\{0,s',k'\}\}$	$(h'+r')^2$	$(h'+r')^2$	h'^2	r'^2
75	$\{\{s',0,0\},\{0,k',l'\},\{0,l',m'\}\}$	$(s'+k')^2$	$(s'+k')^2$	s'^2	k'^2
90	$\{\{e',0,0\},\{0,0,0\},\{0,0,d'\}\}$	$(e')^2$	$(e')^2$	e'^2	0

θ'	$\mathbf{R}_n\ (A_{1g})$	$\sigma^+\sigma^+$	$\sigma^-\sigma^-$	XX	YY
0	$\{\{a',0,0\},\{0,a',0\},\{0,0,b'\}\}$	a'^2	a'^2	a'^2	a'^2
15	$\{\{a',0,0\},\{0,a',0\},\{0,0,b'\}\}$	a'^2	a'^2	a'^2	a'^2
30	$\{\{a',0,0\},\{0,a',0\},\{0,0,b'\}\}$	a'^2	a'^2	a'^2	a'^2
45	$\{\{a',0,0\},\{0,a',0\},\{0,0,b'\}\}$	a'^2	a'^2	a'^2	a'^2
60	$\{\{a',0,0\},\{0,a',0\},\{0,0,b'\}\}$	a'^2	a'^2	a'^2	a'^2
75	$\{\{a',0,0\},\{0,a',0\},\{0,0,b'\}\}$	a'^2	a'^2	a'^2	a'^2
90	$\{\{a',0,0\},\{0,a',0\},\{0,0,b'\}\}$	a'^2	a'^2	a'^2	a'^2

θ'	$\mathbf{R}_n\ (E_{2g})$	$\sigma^+\sigma^+$	$\sigma^-\sigma^-$	XX	YY
0	$\{\{d',0,0\},\{0,-d',0\},\{0,0,0\}\}$	0	0	0	0
15	$\{\{f',g',0\},\{g',h',0\},\{0,0,0\}\}$	0	0	d'^2	d'^2
30	$\{\{f',g',0\},\{g',h',0\},\{0,0,0\}\}$	0	0	d'^2	d'^2
45	$\{\{0,e',0\},\{e',0,0\},\{0,0,0\}\}$	0	0	0	0
60	$\{\{f',g',0\},\{g',h',0\},\{0,0,0\}\}$	0	0	d'^2	d'^2
75	$\{\{f',g',0\},\{g',h',0\},\{0,0,0\}\}$	0	0	d'^2	d'^2
90	$\{\{d',0,0\},\{0,e',0\},\{0,0,0\}\}$	0	0	0	0

φ'	$\mathbf{R}_n\ (A_{1g})$	$\sigma^+\sigma^+$	$\sigma^-\sigma^-$	XX	YY
0	$\{\{a',0,0\},\{0,a',0\},\{0,0,b'\}\}$	0	0	a'^2	a'^2
15	$\{\{a',0,c'\},\{0,b',0\},\{c',0,d'\}\}$	$(a'+b')^2$	$(a'+b')^2$	a'^2	b'^2
30	$\{\{a',0,c'\},\{0,b',0\},\{c',0,d'\}\}$	$(a'+b')^2$	$(a'+b')^2$	a'^2	b'^2
45	$\{\{c',0,b'\},\{0,a',0\},\{b',0,c'\}\}$	$(c'+a')^2$	$(c'+a')^2$	c'^2	a'^2

60	$\{\{a',0,c'\},\{0,b',0\},\{c',0,d'\}\}$	$(a'+b')^2$	$(a'+b')^2$	a'^2	b'^2
75	$\{\{a',0,c'\},\{0,b',0\},\{c',0,d'\}\}$	$(a'+b')^2$	$(a'+b')^2$	a'^2	b'^2
90	$\{\{a',0,0\},\{0,b',0\},\{0,0,b'\}\}$	$(a'+b')^2$	$(a'+b')^2$	a'^2	b'^2

$\boldsymbol{\varphi'}$	$\mathbf{R}_n\ (\boldsymbol{E_{2g}})$	$\sigma^+\sigma^+$	$\sigma^-\sigma^-$	XX	YY
0	$\{\{d',0,0\},\{0,-d',0\},\{0,0,0\}\}$	0	0	0	0
15	$\{\{s',0,l'\},\{0,k',0\},\{l',0,m'\}\}$	$(s'+k')^2$	$(s'+k')^2$	s'^2	k'^2
30	$\{\{h',0,s'\},\{0,r',0\},\{s',0,k'\}\}$	$(h'+r')^2$	$(h'+r')^2$	h'^2	r'^2
45	$\{\{r',0,r'\},\{0,h',0\},\{r',0,r'\}\}$	$(h'+r')^2$	$(h'+r')^2$	r'^2	h'^2
60	$\{\{h',0,s'\},\{0,r',0\},\{s',0,k'\}\}$	$(h'+r')^2$	$(h'+r')^2$	h'^2	r'^2
75	$\{\{s',0,l'\},\{0,k',0\},\{l',0,m'\}\}$	$(s'+k')^2$	$(s'+k')^2$	s'^2	k'^2
90	$\{\{0,0,0\},\{0,f',0\},\{0,0,e'\}\}$	$(f')^2$	$(f')^2$	0	f'^2

Table S2: $\boldsymbol{C_{3v}}$ (3m) for bulk 3R-MoS$_2$

$\boldsymbol{\psi'}$	$\mathbf{R}_n\ (\boldsymbol{A_{1g}})$	$\sigma^+\sigma^+$	$\sigma^-\sigma^-$	XX	YY
0	$\{\{a',0,0\},\{0,a',0\},\{0,0,b'\}\}$	a'^2	a'^2	a'^2	a'^2
15	$\{\{a',0,0\},\{0,b',c'\},\{0,c',d'\}\}$	$(a'+b')^2$	$(a'+b')^2$	a'^2	b'^2
30	$\{\{a',0,0\},\{0,b',c\},\{0,c',d'\}\}$	$(a'+b')^2$	$(a'+b')^2$	a'^2	b'^2
45	$\{\{a',0,0\},\{0,c',b'\},\{0,b',c'\}\}$	$(a'+c')^2$	$(a'+c')^2$	a'^2	c'^2
60	$\{\{a',0,0\},\{0,b',c'\},\{0,c',d'\}\}$	$(a'+b')^2$	$(a'+b')^2$	a'^2	b'^2
75	$\{\{a',0,0\},\{0,b',c'\},\{0,c',d'\}\}$	$(a'+b')^2$	$(a'+b')^2$	a'^2	b'^2
90	$\{\{b',0,0\},\{0,a',0\},\{0,0,b'\}\}$	$(a'+b')^2$	$(a'+b')^2$	b'^2	a'^2

$\boldsymbol{\psi'}$	$\mathbf{R}_n\ (\boldsymbol{E_{2g}})$	$\sigma^+\sigma^+$	$\sigma^-\sigma^-$	XX	YY
0	$\{\{c',0,0\},\{0,d',e'\},\{0,e',0\}\}$	$(c'+d')^2$	$(c'+d')^2$	c'^2	c'^2
15	$\{\{g',0,0\},\{0,h',r'\},\{0,r',s'\}\}$	$(g'+h')^2$	$(g'+h')^2$	g'^2	h'^2
30	$\{\{g',0,0\},\{0,h',r'\},\{0,r',s'\}\}$	$(g'+h')^2$	$(g'+h')^2$	g'^2	h'^2
45	$\{\{f',0,0\},\{0,g',h'\},\{0,h',i'\}\}$	$(g'+f')^2$	$(g'+f')^2$	f'^2	g'^2
60	$\{\{g',0,0\},\{0,h',r'\},\{0,r',s'\}\}$	$(g'+h')^2$	$(g'+h')^2$	g'^2	h'^2
75	$\{\{g',0,0\},\{0,h',r'\},\{0,r',s'\}\}$	$(g'+h')^2$	$(g'+h')^2$	g'^2	h'^2
90	$\{\{d',0,0\},\{0,0,e'\},\{0,e',f'\}\}$	$(d')^2$	$(d')^2$	d'^2	0

$\boldsymbol{\theta'}$	$\mathbf{R}_n\ (\boldsymbol{A_{1g}})$	$\sigma^+\sigma^+$	$\sigma^-\sigma^-$	XX	YY
0	$\{\{a',0,0\},\{0,a',0\},\{0,0,b'\}\}$	a'^2	a'^2	a'^2	a'^2
15	$\{\{a',0,0\},\{0,a',0\},\{0,0,b'\}\}$	a'^2	a'^2	a'^2	a'^2
30	$\{\{a',0,0\},\{0,a',0\},\{0,0,b'\}\}$	a'^2	a'^2	a'^2	a'^2
45	$\{\{a',0,0\},\{0,a',0\},\{0,0,b'\}\}$	a'^2	a'^2	a'^2	a'^2
60	$\{\{a',0,0\},\{0,a',0\},\{0,0,b'\}\}$	a'^2	a'^2	a'^2	a'^2
75	$\{\{a',0,0\},\{0,a',0\},\{0,0,b'\}\}$	a'^2	a'^2	a'^2	a'^2
90	$\{\{a',0,0\},\{0,a',0\},\{0,0,b'\}\}$	a'^2	a'^2	a'^2	a'^2
$\boldsymbol{\theta'}$	$\mathbf{R}_n\ (\boldsymbol{E_{2g}})$	$\sigma^+\sigma^+$	$\sigma^-\sigma^-$	XX	YY
0	$\{\{c',0,0\},\{0,d',e'\},\{0,e',0\}\}$	0	0	c'^2	c'^2

15	$\{\{e',f',h'\},\{f',g',r'\},\{\mathrm{h}',r',0\}\}$	0	0	c'^2	c'^2
30	$\{\{e',f',h'\},\{f',g',r'\},\{\mathrm{h}',r',0\}\}$	0	0	c'^2	c'^2
45	$\{\{0,e',f'\},\{\mathrm{e}',0,f'\},\{f',f',0\}\}$	0	0	0	0
60	$\{\{e,f',h'\},\{f',g',r'\},\{h',r',0\}\}$	0	0	c'^2	c'^2
75	$\{\{e',f',h'\},\{f',g',r'\},\{h',r',0\}\}$	0	0	c'^2	c'^2
90	$\{\{d',0,f'\},\{0,e',0\},\{f',0,0\}\}$	0	0	c'^2	c'^2

φ'	$\mathbf{R}_n\ (A_{1g})$	$\sigma^+\sigma^+$	$\sigma^-\sigma^-$	XX	YY
0	$\{\{a',0,0\},\{0,a',0\},\{0,0,b'\}\}$	a'^2	a'^2	a'^2	a'^2
15	$\{\{a',0,c'\},\{0,b',0\},\{c',0,d'\}\}$	$(a'+b')^2$	$(a'+b')^2$	a'^2	b'^2
30	$\{\{a',0,c'\},\{0,b',0\},\{c',0,d'\}\}$	$(a'+b')^2$	$(a'+b')^2$	a'^2	b'^2
45	$\{\{c',0,b'\},\{0,a',0\},\{b',0,c'\}\}$	$(a'+c')^2$	$(a'+c')^2$	c'^2	a'^2
60	$\{\{a',0,c'\},\{0,b',0\},\{c',0,d'\}\}$	$(a'+b')^2$	$(a'+b')^2$	a'^2	b'^2
75	$\{\{a',0,c'\},\{0,b',0\},\{c',0,d'\}\}$	$(a'+b')^2$	$(a'+b')^2$	a'^2	b'^2
90	$\{\{a',0,0\},\{0,b',0\},\{0,0,b'\}\}$	$(a'+b')^2$	$(a'+b')^2$	a'^2	b'^2

φ'	$\mathbf{R}_n\ (E_{2g})$	$\sigma^+\sigma^+$	$\sigma^-\sigma^-$	XX	YY
0	$\{\{c',0,0\},\{0,d',e'\},\{0,e',0\}\}$	0	0	c'^2	c'^2
15	$\{\{\mathrm{s}',k',m'\},\{k',l',n'\},\{m',n',o'\}\}$	$(s'+l')$	$(s'+l')$	s'^2	l'^2
30	$\{\{r',s',l'\},\{s',k',m'\},\{l',m',n'\}\}$	$(r'+k')^2$	$(r'+k')^2$	r'^2	k'^2
45	$\{\{s',g',s'\},\{g',h',r'\},\{s',r',s'\}\}$	$(s'+h')$	$(s'+h')$	s'^2	h'^2
60	$\{\{r',s',l'\},\{s',k',m'\},\{l',m',n'\}\}$	$(r'+k')^2$	$(r'+k')^2$	r'^2	k'^2
75	$\{\{s',k',m'\},\{k',l',n'\},\{m',n',o'\}\}$	$(s'+l')$	$(s'+l')$	s'^2	l'^2
90	$\{\{0,c',0\},\{c',d',0\},\{0,0,e'\}\}$	$(d')^2$	$(d')^2$	0	d'^2

17. References

(1). Zhang T.; He Y.; Lv Q.; Chen F.; One-Step CVD Growth and Interlayer Coupling Characteristics of Twisted MoS2/MoS2/MoS2 Homotrilayers. *J phys. Chem. C* **2023**, 127, 23420- 23427. https://doi.org/10.1021/acs.jpcc.3c05832.

(2). Zhang X.; Qiao X.-F.; Shi W.; Wu J.-B.; Jiang D.-S.; Tan P.-H.; Phonon and Raman scattering of two-dimensional transition metal dichalcogenides from monolayer, multilayer to bulk material. *Chem. Soc. Rev.* **2015**, 44, 2757-2785. https://doi.org/10.1039/C4CS00282B.

(3). Aroyo, M. I.; Kirov, A.; Capillas, C.; Perez-Mato, J. M.; Wondratschek, H. Bilbao Crystallographic Server. II. Representations of Crystallographic Point Groups and Space Groups. *Acta Crystallographica Section A* **2006**, *62* (2), 115–128. https://doi.org/https://doi.org/10.1107/S0108767305040286.

(4) Aroyo, M. I.; Perez-Mato, J. M.; Capillas, C.; Kroumova, E.; Ivantchev, S.; Madariaga, G.; Kirov, A.; Wondratschek, H. Bilbao Crystallographic Server: I. Databases and Crystallographic Computing Programs. **2006**, *221* (1), 15–27. https://doi.org/doi:10.1524/zkri.2006.221.1.15.

(5) Aroyo, M. I.; Perez-Mato, J. M.; Orobengoa, D.; Tasci, E.; de la Flor, G.; Kirov, A. Crystallography Online: Bilbao Crystallographic Server. *Bulg. Chem. Commun* **2011**, *43* (2), 183–197.